Laser-induced optical satellite line profiles in a helium plasma*

D. Prosnitz,† D. W. Wildman, and E. V. George‡
Department of Physics and Research Laboratory of Electronics, Massachusetts Institute of Technology, Cambridge, Massachusetts 02139
(Received 25 August 1975)

We have observed several different satellite transitions among HeI excited states. These satellites were induced by large, near-resonant, spatially inhomogeneous electric fields. A simple theory was proposed to explain the line shape of both the satellite and the allowed line based on the rotating-wave approximation. The plasma was contained in a dielectric waveguide and the laser mode pattern inside the guide was calculated and incorporated into the line-shape function. It was shown that excellent agreement between theory and experiment could be obtained over a wide range of experimental parameters. Agreement was very good in regimes where perturbation theory fails. We also observed that at high field strengths the Stark shift of the allowed component was less than the three-level theory predicted. We attribute this error to the fact that we have ignored all of the remaining levels of the HeI system.

I. INTRODUCTION

Detailed analysis of the spectral-line profiles emitted by plasmas has been extensively used to ascertain such macroscopic plasma properties as density and temperature. The theoretical development in many of the calculations which pertains to the effects of plasma density on the line shapes relies on the use of a dc ion microfield (the so-called quasistatic approximation). The electron effects are then treated by using a perturbation analysis. In general, such calculations do not incorporate the fields associated with the presence of collective oscillations in the plasma. It is clear that allowing for such phenomena in the line-shape description will allow one to deduce experimentally both the amplitude and the frequency spectrum of these collective fluctuations. In addition to changes in the line profiles, it is also possible, under appropriate conditions, to observe additional spectral lines from the plasma (called satellites). The shape and intensity of the satellites are interrelated with the precise nature of the collective phenomena.

In this work, we shall discuss both the theoretical and the experimental characteristics of the satellite-line profiles emitted from a helium target plasma. These lines are the result of the application of a high-frequency, narrow-bandwidth electric field from a CO_2 laser. We begin by reviewing briefly the past work in this area, and then proceed to discuss our results.

In 1961 Baranger and Mozer[1] proposed using the high-frequency Stark effect as a diagnostic method of studying the high-frequency oscillations in a plasma. They considered the three-level system shown in Fig. 1. The parity of the levels are such that transitions between levels A-B and B-C are allowed by electric-dipole radiation whereas the transition between levels A-C is forbidden. The presence of a perturbing electric field mixes levels A and B so that for the case of a dc field, for example, the forbidden line at the frequency $(E_A - E_C)/\hbar$ (where E_i represents the energy of the appropriate level and $\hbar$ is Planck's constant) is observed in the emission spectra. If, however, the field oscillates at a frequency Ω, satellite lines (additional spectral lines that flank the forbidden line) may be observed at frequencies $(E_A - E_C)/\hbar \pm \Omega$. As a first approximation, the precise nature of the electric field is not important. However, Baranger and Mozer showed that if the field is produced by plasma oscillations at the plasma frequency $\Omega = \omega_p = (ne^2/m\epsilon_0)^{1/2}$, where n is the electron density and the other parameters have their usual connotation, then the separation between the satellite lines can be used to ascertain the plasma density. Using a standard second-order perturbation calculation, they derived the ratio of the integrated

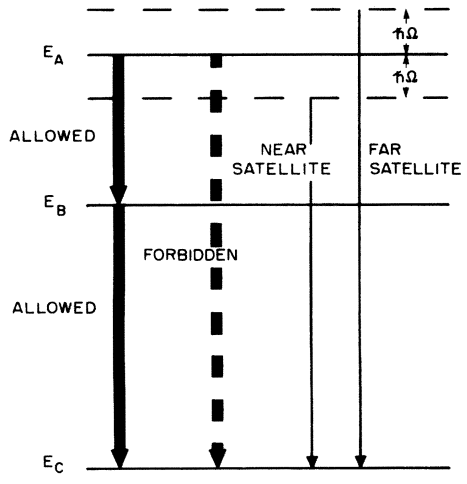

FIG. 1. Three-level atomic system perturbed by an electric field at frequency Ω.

intensity of the satellite line to that of the associated allowed line. This ratio, denoted by $S_{\pm}$, can be written

$$S_{\pm}=\frac{\epsilon^2\langle A|d|B\rangle_m^2}{2(E_A-E_B\pm\hbar\Omega)^2}G(l_A,l_B). \tag{1.1}$$

In this equation ϵ is the rms electric field at the frequency Ω, $\langle A|d|B\rangle$ the dipole moment between states A and B, and the subscript m denotes the average over magnetic quantum numbers. $G(l,l')$ is given by

$$G(l,l')=\max(l,l')/(2l+1). \tag{1.2}$$

Here l is the orbital quantum number for the upper state of the allowed line (B-C) and l' is the orbital quantum number for the upper state of the forbidden line (A-C).

Equation (1.1) represents an average over randomly polarized ϵ field directions. Polarization and magnetic field effects may easily be included.[2,3] In principle, one can determine both the magnitude and the frequency of the perturbing electric field; however, it is important to point out that the result given in Eq. (1.1) is not valid at high field strengths and/or near resonant frequencies, and it does not include the Stark shift of the energy levels owing to the presence of the oscillating electric field. In addition, multiple-frequency, inhomogeneous electric fields and plasma (dc) line broadening and shifts are not included.

Several authors have advanced the work of Baranger and Mozer[4] and a number of experiments have demonstrated that a perturbation treatment of the problem is inadequate.[5,3] Hicks, Hess, and Cooper[3] developed a theory that is able to predict the observed spectrum of microwave satellites extremely well. Unfortunately, their theory necessitates long numerical computations which makes it extremely cumbersome to calculate the satellite spectrum induced by spatially inhomogeneous or multiple-frequency fields. Furthermore, they assumed that the upper states had equal populations, a fact that is certainly not in general true. Hamada[6] modified the result of Baranger and Mozer to incorporate unequal excited-state populations. He did not allow for induced transitions between these levels. We would like a means of calculating the satellite spectrum that incorporates all of these effects so that we might be able to predict the satellite spectrum in nonequilibrium plasmas.

In Sec. II we outline a theory for calculating the satellite-line shapes based on the rotating-wave approximation, first used by Rabi.[7] We present a closed-form solution in terms of a complex angle χ which includes both unequal populations of the various atomic states and collision-induced dephasing of the interacting states. In addition, a spatially inhomogeneous electric field is included and the limits of validity of the solution are discussed.

In Sec. III we describe an experiment in which optical satellites induced by a CO_2 laser are observed in a helium plasma.[5] Finally, in Sec. IV we show how the theory developed in Sec. II correctly predicts the observed satellite profiles in the presence of spatially inhomogeneous, near-resonant, laser fields.

II. THEORY

In 1955, Autler and Townes[8] examined the effect of a rapidly varying electric field on an atomic system. They demonstrated that Schrödinger's equation for a two-level system could be solved for all values of perturbing field strength and frequencies (as long as the field was monochromatic) in terms of an infinitely continued fraction. Multiple photon effects were revealed and studied in the microwave region. These multiple photon transitions were in fact the satellites that Baranger and Mozer discussed later in reference to plasma satellites.

We now proceed with a calculation of the satellite-line shape based on the rotating-wave approximation. We take for our model the level scheme illustrated in Fig. 1. The profile of a spectral line emitted when the system undergoes a transition may be expressed as follows[9]:

$$P(\omega)=\frac{4\omega^4}{3c^3}\frac{1}{2\pi T}\left|\int_0^T dt e^{i\omega t}\langle\psi_f|d|\psi_i(\epsilon,t)\rangle\right|^2_{\text{avg}}, \tag{2.1}$$

where $P(\omega)$ is the power emitted per unit frequency at a frequency ω, c is the speed of light, and $|\psi_f\rangle$ and $|\psi_i(\epsilon,t)\rangle$ are the wave functions for the final and initial states of the atom. As before, d is a dipole operator for the transition and avg refers to an average over all emitting atoms. It is important to note that we have written $|\psi_i\rangle$ as a function of the perturbing electric field while we have assumed $|\psi_f\rangle$ is unaffected by the perturbing field. This is usually an excellent approximation as the final state C is much more tightly bound than the upper states A and B. If we were considering a stimulated process, such as the Raman laser, we would have to allow for perturbations of $|\psi_f\rangle$ as well. T is a characteristic time over which the measurement is made and typically is the correlation time for an atomic transition. If we assume that the oscillations are damped for times $t>T$, the limits on the integration may be extended to infinity.

The inclusion of a spatially inhomogeneous electric field proceeds by introducing the field distribution function $W(\epsilon)$ normalized in such a manner that

$$\int_0^\infty W(\epsilon)\,\epsilon^2 d\epsilon = 1. \tag{2.2}$$

The precise form of $W(\epsilon)$ obviously depends on the experiment being performed. In Appendix A we derive $W(\epsilon)$ for the specific experiment discussed in Sec. III.

It is important to note that we have not included ion broadening in Eq. (2.1). In actuality, $|\psi_f\rangle$ and $|\psi_i\rangle$, should be written as functions of the ion electric field F. In most cases of interest the ion field may be included by a simple extension of the results described below.[10]

We can now write Eq. (2.1) in the following manner:

$$P(\omega) = \frac{4\omega^4}{3c^3}\frac{1}{2\pi T}\int_0^\infty W(\epsilon)\,d\epsilon \times \left|\int_0^\infty dt\, e^{i\omega t}\langle\psi_f|d|\psi_i(\epsilon,t)\rangle\right|^2_{\text{avg}}. \tag{2.3}$$

We now proceed writing the initial and final wave functions in terms of the time-independent, unperturbed wave functions $|\phi\rangle$ for the three-level scheme of Fig. 1,

$$|\psi_i(t,\epsilon)\rangle = a(t,\epsilon)|\phi_A\rangle + b(t,\epsilon)|\phi_B\rangle,$$
$$|\psi_f(t,\epsilon)\rangle = c(t)|\phi_c\rangle. \tag{2.4}$$

Since we have assumed that the final state is not perturbed by the electric field, we can write $c(t) = \exp(-iE_c t/\hbar)$. Equation (2.3) can now be written

$$P(\omega) = \frac{4\omega^4}{3c^3}\frac{1}{2\pi T}\int_0^\infty W(\epsilon)\,d\epsilon\,|d_{BC}|^2\,|B(S)|^2_{\text{avg}}, \tag{2.5}$$

where $B(S)$ is the Laplace transform of $b(t)$ and $S = -i(\omega + E_c/\hbar)$ (Schrödinger representation). We will adopt the convention that capital letters represent Laplace transforms of time-variant quantities that are denoted by small letters.

We now write Schrödinger's equation in the interaction representation,

$$-\frac{\hbar}{i}\frac{\partial|\psi_i\rangle}{\partial t} = H_{AB}|\psi_i\rangle, \tag{2.6}$$

where $H_{AB} = \sqrt{2}\,\epsilon d_{AB}\cos\Omega t$ and ϵ is the rms electric field at frequency Ω. The coupled equations for $a(t)$ and $b(t)$ may now be written as

$$\frac{da}{dt} + \gamma_A a = -\frac{i}{\hbar}d_{AB}e^{i(E_A-E_B)t/\hbar}(\sqrt{2}\,\epsilon)\frac{e^{i\Omega t}+e^{-i\Omega t}}{2}b, \tag{2.7a}$$

$$\frac{db}{dt} + \gamma_B b = -\frac{i}{\hbar}d_{BA}e^{-i(E_A-E_B)t/\hbar}(\sqrt{2}\,\epsilon)\frac{e^{-i\Omega t}+e^{i\Omega t}}{2}a, \tag{2.7b}$$

where $d_{AB} = \langle\phi_A|d|\phi_B\rangle$. We include a phenomenological damping constant γ to account for broadening of the interacting levels. Implicit in these equations is the assumption that γ_A and γ_B are independent of the high-frequency electric field.

We must now consider the initial conditions appropriate for Eqs. (2.7). At $t \leq 0$, the laser field is off. Any given atom is initially in either state $|\phi_A\rangle$ or $|\phi_B\rangle$. We can state that the atom has a probability a_0^2 of being in state A and b_0^2 of being in state B. Rather than solve Eqs. (2.7) for two different sets of boundary conditions ($a_0 = 1$, $b_0 = 0$ and $a_0 = 0$, $b_0 = 1$) and then perform the appropriate ensemble average, we choose the equivalent method of solving Eqs. (2.7) with the boundary conditions $a(0) = a_0$ and $b(0) = b_0 e^{i\theta}$ and then average over θ. This ensures that there are no coherent effects induced by the initial conditions, i.e., it ensures that the atom is correctly described as being either in state A or state B. We assume that the net rate of excitation to states A and B from all other states is unchanged in the presence of the oscillating electric field.

The coupled equations [Eqs. (2.7)] in conjunction with their initial conditions are not solvable in closed form. There are essentially three methods of finding approximate solutions. A perturbation expansion, the usual method, is totally inappropriate for the near-resonant, high-field-strength situation considered here. The Floquet method[11] necessitates long numerical calculations and may, in fact, become unmanageable. A third technique is to employ Rabi's rotating-wave approximation. This is often done in the field of quantum optics,[12] but rarely in plasma spectroscopy. The rotating-wave approximation assumes that one may write the Hamiltonians

$$H_{AB} = \tfrac{1}{2}d_{AB}(\sqrt{2}\,\epsilon)e^{i\Omega t} \tag{2.8a}$$

and

$$H_{BA} = \tfrac{1}{2}d_{BA}(\sqrt{2}\,\epsilon)e^{-i\Omega t}. \tag{2.8b}$$

This approximation is valid as long as the following three conditions are satisfied:

$$R = \frac{E_A - E_B - \hbar\Omega}{E_A - E_B + \hbar\Omega} \ll 1, \tag{2.9a}$$

$$|H_{AB}|/2\hbar\Omega \ll 1, \tag{2.9b}$$

$$|H_{AB}|/2\hbar(E_A - E_B) \ll 1. \tag{2.9c}$$

Equation (2.9a) states that one must be near resonance, i.e., one rotating wave must be nearly on resonance with the dipole moment ($d_{AB}e^{i(E_A-E_B)t/\hbar}$), while the counter-rotating wave is far from resonance. Equations (2.9b) and (2.9c) are merely a restatement of the Bloch-Siegert[13] condition that the perturbation caused by the counter-rotating wave must be small. If these conditions are not

violated, and the rotating-wave approximation is made, Schrödinger's equation may be solved in closed form.

Which of three methods of solution is chosen depends on the exact nature of the phenomenon to be described. If $H_{AB}/(E_A - E_B \pm \hbar\Omega)$ is small, the perturbation solution is perfectly adequate. At the opposite extreme, if $H_{AB}/(E_A - E_B \pm \hbar\Omega)$ is not small, and conditions (2.9) are not met, one is forced to use the Floquet form of solution. We use the rotating-wave approximation, which is a compromise between these two techniques. As a result, we are not restricted to the low field strengths required by the perturbation technique, nor are we hindered by the complexities of the Floquet treatment. The disadvantage is that we can operate only in a regime where Eqs. (2.9) are valid. Each situation must be examined to determine if the expected field strengths, field frequencies, and energy-level separations are consistent with Eqs. (2.9). A judicious choice of energy levels usually allows one to use the rotating-wave approximation. Higher-order satellites are ignored, since as can be seen from Eqs. (2.9) their intensity is small and they are well removed from the main features of the spectrum.

Using the rotating-wave approximation we can rewrite Eqs. (2.7) in the following form:

$$\frac{da}{dt} + \gamma_A a = -ib\,\frac{d_{AB}}{\hbar}\,\frac{\sqrt{2}}{2}\,\epsilon\, e^{i\Delta t} \tag{2.10a}$$

and

$$\frac{db}{dt} + \gamma_B b = -ia\,\frac{d_{BA}}{\hbar}\,\frac{\sqrt{2}}{2}\,\epsilon\, e^{-i\Delta t}, \tag{2.10b}$$

where

$$\Delta = (E_A - E_B)/\hbar - \Omega. \tag{2.10c}$$

Taking the Laplace transforms of Eqs. (2.10a) and (2.10b) and rearranging terms, it can be shown that

$$\frac{A(S)}{a_0} = \frac{S + \gamma_B - i\Delta - (id_{AB}b_0 e^{i\theta}/\hbar a_0)\,\frac{1}{2}\sqrt{2}\,\epsilon}{[S + \frac{1}{2}(\gamma_B + \gamma_A - i\Delta)]^2 + \beta^2} \tag{2.11a}$$

and

$$\frac{B(S)}{b_0 e^{i\theta}} = \frac{S + \gamma_A + i\Delta - (id_{BA}a_0 e^{-i\theta}/\hbar b_0)\,\frac{1}{2}\sqrt{2}\,\epsilon}{[S + \frac{1}{2}(\gamma_A + \gamma_B + i\Delta)]^2 + \beta^2}, \tag{2.11b}$$

where

$$\beta^2 = \epsilon^2 d^2/2\hbar^2 + \tfrac{1}{4}[\Delta + i(\gamma_B - \gamma_A)]^2. \tag{2.11c}$$

Upon examining these equations one recognizes that a considerable simplification is possible with the introduction of the complex angle χ,[14,15] defined as

$$\tan\chi = \sqrt{2}\,\epsilon\,(d_{BA}d_{AB})^{1/2} \times[\Delta - i(\gamma_B - \gamma_A)]/\hbar[\Delta^2 + (\gamma_B - \gamma_A)^2] \tag{2.12}$$

which when substituted into Eq. (2.11c) yields

$$\beta_\pm = \pm\tfrac{1}{2}\sec\chi[\Delta + i(\gamma_B - \gamma_A)]. \tag{2.13}$$

The plus (minus) root is to be used in Eq. (2.11a) (Eq. (2.11b)).

χ is well defined by Eq. (2.12) as long as $|\Delta| > 0$, and we restrict ourselves to the principal value $2\pi \geq \mathrm{Re}(\chi) \geq 0$. At this stage, in order to simplify the results, we shall assume that $\gamma_A = \gamma_B \equiv \gamma$. This allows us to neglect the imaginary part of χ. We can then rewrite Eqs. (2.11a) and (2.11b) as follows:

$$\frac{A_S}{a_0} = \frac{\cos^2\tfrac{1}{2}\chi - (b_0/a_0)\,\tfrac{1}{2}(\sin\chi)e^{i\theta}}{(S + i\Delta_S) + \gamma} + \frac{\sin^2\tfrac{1}{2}\chi + (b_0/a_0)\,\tfrac{1}{2}(\sin\chi)e^{i\theta}}{(S - i\Delta_S - i\Delta) + \gamma}, \tag{2.14a}$$

$$\frac{B_S}{b_0 e^{i\theta}} = \frac{\cos^2\tfrac{1}{2}\chi - (a_0/b_0)\,\tfrac{1}{2}(\sin\chi)e^{-i\theta}}{(S - i\Delta_S) + \gamma} + \frac{\sin^2\tfrac{1}{2}\chi + (a_0/b_0)\,\tfrac{1}{2}(\sin\chi)e^{-i\theta}}{(S + i\Delta_S + i\Delta) + \gamma}, \tag{2.14b}$$

where the Stark shift $\Delta_s \equiv -\tfrac{1}{2}\Delta(1 - \sec\chi)$. We further assume that $\gamma/(\Delta + 2\Delta_s) \ll 1$, which is almost always true. This allows us to ignore the cross terms and write

$$A(S)A^*(S) = \frac{\eta_a}{(\Delta_s - \omega)^2 + \gamma^2} + \frac{\zeta_a}{(\Delta_s + \Delta + \omega)^2 + \gamma^2}, \tag{2.15a}$$

$$B(S)B^*(S) = \frac{\eta_b}{(\omega + \Delta_s)^2 + \gamma^2} + \frac{\zeta_b}{(\omega - \Delta_s - \Delta)^2 + \gamma^2}, \tag{2.15b}$$

where

$$\eta_a = (\cos^2\tfrac{1}{2}\chi)(a_0^2\cos^2\tfrac{1}{2}\chi + b_0^2\sin^2\tfrac{1}{2}\chi), \tag{2.16a}$$

$$\zeta_a = (\sin^2\tfrac{1}{2}\chi)(a_0^2\sin^2\tfrac{1}{2}\chi + b_0^2\cos^2\tfrac{1}{2}\chi). \tag{2.16b}$$

The corresponding expressions for η_b and ζ_b are obtained by interchanging a_0^2 and b_0^2 in (2.16). In Eq. (2.15a) we have chosen our zero of energy to be $E_A - E_C$; in Eq. (2.15b) we chose $E_B - E_C$ to represent zero energy. Since transitions from A to C are not allowed, AA^* does not contribute to the line shape. We will therefore discuss only Eq. (2.15b). As we shall see, Eq. (2.15b) will lead to two spectral lines separated in frequency by $2\Delta_s + \Delta$. The first term becomes the allowed line and the second term its associated satellite. They show the expected Stark repulsion, one shifting up in frequency by Δ_s, the other down by Δ_s. If $a_0^2 = b_0^2$

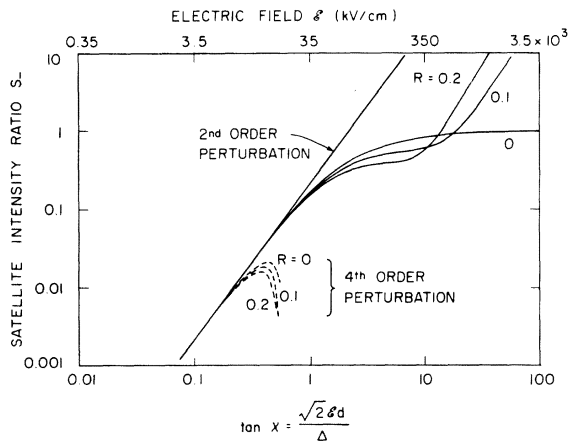

FIG. 2. S_- as computed by (i) second-order perturbation theory, (ii) a fourth-order perturbation treatment, (iii) Eq. (2.15b) for the case $R=0$ and $a_0^2=b_0^2$, and (iv) the next-order Autler-Townes solution for the case $R\neq 0$. The electric field strengths shown are for the helium system discussed in Sec. III.

(equal initial populations) we find $S_- = \tan^2\frac{1}{2}\chi$. In the small-field limit ($\chi \ll \frac{1}{2}\pi$), and after averaging over magnetic quantum numbers, this reduces to the result of Baranger and Mozer, as expected. In the limit $\chi \to \frac{1}{2}\pi$, the levels (in conjunction with the electromagnetic field) become degenerate and $S_- \to 1$.

As pointed out by Autler and Townes,[8] the counter-rotating wave (neglected in the rotating-wave approximation) will alter this solution somewhat. The magnitude of this effect is proportional to R given in Eq. (2.9a). In Fig. 2 we plot S_- [cf. Eq. (1.1) and subsequent discussion] as a function of perturbing field strength as computed by (i) Baranger and Mozer, (ii) a fourth-order perturbation treatment,[16] (iii) Eq. (2.15b) for the case $R=0$ and $a_0^2=b_0^2$, and (iv) the next-order Autler-Townes solution [cf. Eq. (42) of their manuscript] for the case $R\neq 0$. The field strengths presented are for the particular He system which we have experimentally examined. From Fig. 2, we see that as R becomes small, the maximum permissible field becomes larger before the theory becomes invalid. The peak fields reached in our experiment are approximately 650 kV/cm but as R is only 0.014, the rotating-wave approximation is entirely satisfactory. It can be seen that the perturbation treatments, both second and fourth order, are entirely unsatisfactory at high field strengths. It is important to point out that the Bloch-Siegert shift is recoverable from a perturbation analysis of Eq. (2.15b).

In Fig. 3 we have plotted Δ_s/Δ as a function of $\tan\chi(\epsilon)$ for several values of R. The $R=0$ solution is seen to be quadratic in field strength for small fields and linear at large field strengths. If $R\neq 0$, the discrepancy between the rotating-wave approximation and the solution corrected for the counter-rotating wave becomes large as ϵ becomes large, as is evident from both Figs. 2 and 3. This occurs as both Eqs. (2.10b) and (2.10c) fail. From this we see that for large field strengths the counter-rotating wave cannot be ignored.

If $a_0^2\neq b_0^2$ we can divide both the allowed line and the satellite into two components [cf. (2.15b)]. The allowed line is seen to consist of the terms $b_0^2\cos^4\frac{1}{2}\chi$ and $a_0^2(\cos^2\frac{1}{2}\chi)(\sin^2\frac{1}{2}\chi)$. The first term represents the initial population of the level diminished by both the satellite and transitions to level B, while the second represents the contributions from transitions from level A to level B. The satellite is composed of the terms $a_0^2(\sin^2\frac{1}{2}\chi)\times(\cos^2\frac{1}{2}\chi)$ and $b_0^2\sin^4\frac{1}{2}\chi$. The first term represents the population of level A times the two-photon rate, while the second represents the contribution to the satellite from transitions from level B to level A. Note that if $a_0^2=b_0^2$ there is no net transfer of excitation, as expected.

Using Eqs. (2.5), (2.15), and (2.16), we can finally write the line shape as

$$P(\omega)=\frac{4\omega^4}{3c^3}\int_0^\infty W(\epsilon)\,d\epsilon\,|d_{BC}|^2\frac{\gamma}{2\pi}\left(\frac{\eta_b}{[\omega+\Delta_s-(E_B-E_c)/\hbar]^2+\gamma^2}+\frac{\zeta_a}{[\omega-\Delta_s+\Omega-(E_A-E_C)/\hbar]^2+\gamma^2}\right), \tag{2.17}$$

where we have written $\gamma=1/T$, $\chi=\chi(\epsilon)$, and $\Delta_s=\Delta_s(\epsilon)$.

In actual use, we must include the multiplicities of the levels when computing the line shape. Because this depends on the actual system studied, we will defer discussion of this point until Sec. IV where we present our experimental results.

III. EXPERIMENTAL SETUP

As discussed previously, our objective was to study the details of the line profiles of optical satellites induced by large, near-resonant, high-frequency electric fields. In particular, we wished to see if the theory outlined in Sec. II is adequate when the standard perturbation techniques are no longer valid. To simplify the analysis, we sought to study the satellites induced by a narrow-bandwidth perturbing field. In addition, we chose those satellites that occur in a spectral region free from additional spectral lines so that their profiles need not be deconvolved from the wings of any nearby lines.

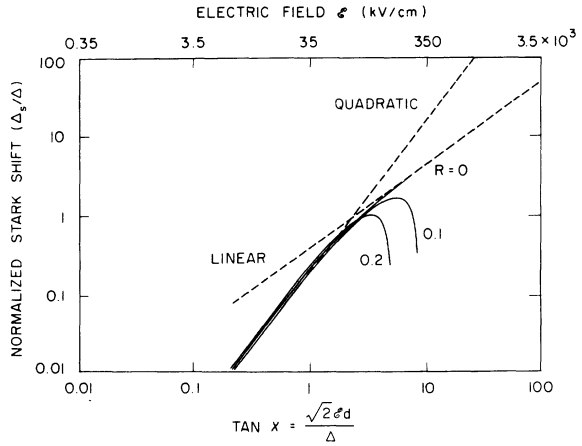

FIG. 3. Electric-field dependence of the Stark shift as computed by the rotating-wave approximation [cf. Eq. (2.14) for $R=0$] and the next-order Autler-Townes solution for the case $R \neq 0$. At low field strengths Δ_s/Δ is proportional to ϵ^2 and at high field strengths Δ_s/Δ becomes linear in ϵ.

We used the optical pulse from a CO_2 laser as the field source. In order to maximize the satellite intensity and to operate in a region where perturbation theory fails, it is desirable to minimize Δ, the energy deficit. We have therefore chosen to study the $2\,^3P$-$4\,^3S$ and $2\,^3S$-$4\,^3P$ transitions of He I. The relevant energy levels are shown in Fig. 4. Here the $4\,^3P$ and $4\,^3S$ levels (corresponding to states A and B of Fig. 1) are separated by 919 cm^{-1} whereas for the $P(20)$ transition of the 10.6-μm 961-cm^{-1} band in the CO_2 laser the photon energy ($\hbar\Omega$) is 944 cm^{-1}. Using the relationships given by Eqs. (2.9), it is clear that the use of the rotating-wave approximation (see Sec. II) is appropriate. In Fig. 4, we have indicated two different near satellites, one corresponding to a two-photon transition between the $2\,^3S$-$4\,^3S$ states and the other corresponding to a two-photon transition between the $2\,^3P$-$4\,^3P$ states. Their corresponding allowed transitions are $2\,^3P$-$4\,^3S$ (4713 Å) and $2\,^3S$-$4\,^3P$ (3188 Å). The Stark shifts of the upper states are also shown in Fig. 4. We thus have two independent means of measuring the strength of the perturbing field and a self-consistent method of confirming the theoretical predictions of Sec. II.

The experimental apparatus is diagrammed in Fig. 5. We have constructed a moderate power TEA CO_2 laser to act as the field source. The laser operates at 30 Hz and produces 300-mJ pulses with 0.2–0.4 of the total energy in a 200-nsec main pulse. The shot-to-shot variation of the laser power is less than 10%. The laser cavity is 1.75 m long and usually consists of a Bausch and Lomb diffraction grating and a 10-m radius of curvature, 90%-reflectivity germanium output mirror. The system will lase on approximately 30 different CO_2 transitions in both the 10.6-μm 961-cm^{-1} and 9.6-μm 1063-cm^{-1} bands. We can also operate the laser in a scheme of two spatially independent optical cavities, both operating on the same gain medium.[10] Because one cavity is tunable, we are capable of producing two simultaneous laser pulses at different frequencies. Except for one instance, the data presented in this paper were obtained using the single-cavity configuration.

The laser output radiation is reflected from a movable mirror (see Fig. 5) either into an Optical Engineering CO_2 spectrum analyzer which measures the laser wavelength or onto a 12.5-cm-focal-length germanium lens. The lens optically couples the laser output into one end of a quartz capillary tube 5 cm long and 550 μm in diameter. The capillary has tapered ends to minimize discharge instabilities. The coupling of the radiation into the discharge tube depends on the spot size (100 μm) of the laser at the focal point of the lens. The capillary acts as a dielectric waveguide for the purpose of radiation transport. The natural modes of these guides have been calculated by numerous workers (see Appendix A).

A helium plasma is created by passing a 5-μsec current pulse through the same quartz capillary. A five-section pulse-forming network is coupled to the discharge tube by an impedance-matching

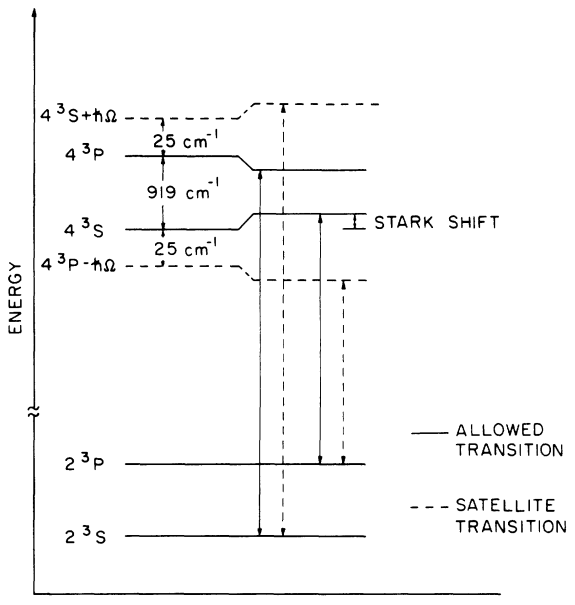

FIG. 4. Partial helium energy-level diagram perturbed by a CO_2 laser field operating on the $P(20)$ transition of the 10.6 μm branch (944 cm^{-1}).

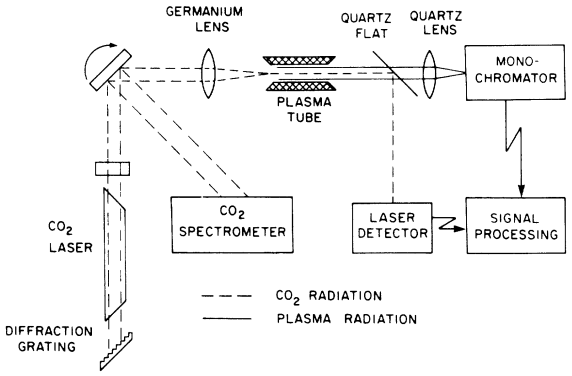

FIG. 5. Experimental apparatus as viewed from above.

transformer to create a flat current pulse. Standard high-vacuum techniques are used to evacuate the discharge tube and then refill it with spectroscopic-grade helium.

A quartz flat, placed at the far end of the discharge tube, acts as a filter, separating the infrared laser radiation from the visible plasma radiation. The laser radiation passes onto a liquid-nitrogen cooled gold-doped germanium detector. The visible radiation is imaged by a quartz lens onto the slits of a 0.5-m motor-driven scanning monochromator (Jarell Ash Model 82-020). The monochromator was modified so that it would scan at speeds as slow as 0.125 Å/min. The systematic sine bar error of the monochromator was measured and found to have a period of ≈50 Å with an amplitude of ±1.4 Å. A linear approximation to the sinusoidally varying error was made in each region of interest. The radiation from the monochromator passed onto an RCA 8850 photomuliplier. The response of the photomultiplier-monochromator was calibrated in the standard manner. This allowed us to compare accurately the intensities of widely separated emission lines. The photomultiplier signal was amplified and delayed before reaching the gated boxcar integrator (PAR Model 160). A signal from the laser detector was used to trigger the gate of the integrator. The output was displayed on a strip chart recorder. The boxcar gate was typically 200 nsec wide and was temporally positioned about the peak of the laser pulse. Narrower gates were used in conjunction with the automatic-scan mode of the boxcar in order to examine the temporal evolution of both the optical satellites and the associated allowed lines. All of the equipment was enclosed in a screened room.

The plasma density and electron temperature were measured spectroscopically. The electron temperature was found to be approximately 3 eV by comparing the integrated intensity of the He I 5876-Å line to that of the He II 4686-Å line.[17] The density was estimated by comparing the intensity of the He I 4922-Å ($2\,^1P$-$4\,^1D$) line to the intensity of its forbidden component ($2\,^1P$-$4\,^1F$).[18]

The theory outlined in Sec. II can be modified to yield an estimate of the line shape of the $2\,^1P$-$4\,^1F$, -$4\,^1D$ transitions.[10] Figure 6 shows a comparison of that theory (convolved with the measured instrument function) with an electron density of 7×10^{14} cm^{-3}, an electron temperature of 3 eV, and a neutral temperature of 0.05 eV and data taken at a discharge current of 4 A and a pressure of 2.2 Torr. A one-parameter fit was done to determine the density.

The measurements of electron density discussed above were performed without the CO_2 laser radiation. At the lower densities (5×10^{14} cm^{-3}) the laser has a negligible effect on the gross plasma properties. Neither the He II 4686-Å line nor the He I 4922-Å line showed any laser-induced change in intensity. The He I 5876-Å line did change by almost 20% but it was felt that this was not caused by an alteration of the plasma temperature. (The reason for this alteration is not clearly understood.) No significant laser absorption was observed until the discharge current was increased above 150 A, corresponding to an electron density $n\cong10^{16}$ cm^{-3}. All of the data presented in this paper were obtained at the lower electron density $n\cong5\times10^{14}$ cm^{-3}.

A typical photomultiplier signal is shown in Fig. 7(a). The monochromator has been set to the peak of the 4713-Å ($2\,^3P$-$4\,^3S$) line with a slit width of 45 μm corresponding to a resolution of 0.75 Å. The laser was not operating when the picture was taken. Figure 7(b) shows the light emitted from the same portion of the spectrum when the laser is allowed to interact with the plasma. As reported earlier, the intensity of the line is severely diminished. A comparison of the laser pulse shape [Fig. 7(c)] and the perturbation of the intensity of

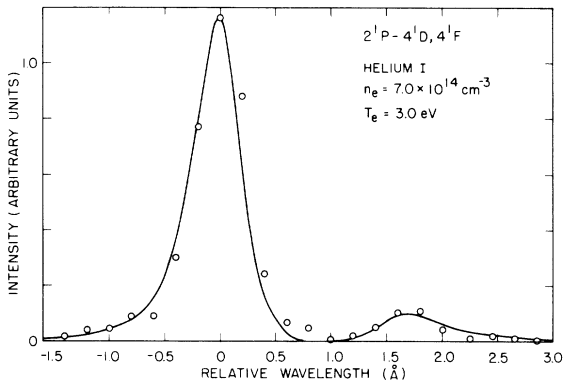

FIG. 6. Comparison of the theoretical line shapes (○) and the measured profiles of the He I 4922-Å allowed line and its forbidden component.

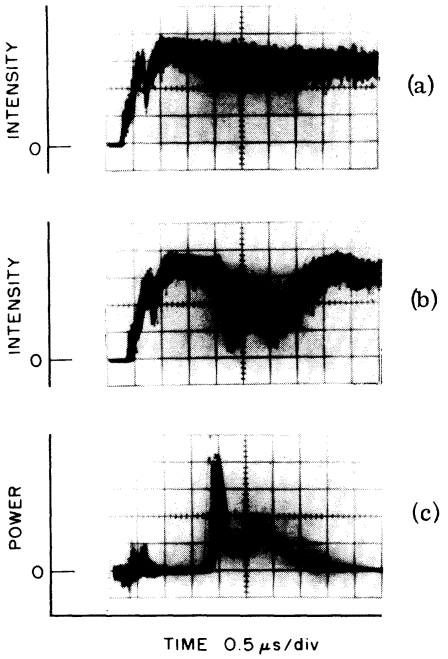

FIG. 7. Oscilloscope traces of (a) 4713-Å light pulse unperturbed by the laser (top trace), (b) 4713-Å light pulse perturbed by the laser (middle trace), and (c) laser pulse shape (bottom trace).

the 4713-Å line would indicate that the change is roughly proportional to the laser energy and occurs on the same time scale as the laser pulse. However, part of the change in intensity shown in Fig. 7(b) is because of the laser-induced Stark shift moving the line out of the bandwidth of the monochromator. The actual change in the integrated intensity is ~40%. The reasons for this are discussed more completely in Sec. IV. Previous workers have also studied "light" shifts and changes in intensity.[19-21]

A typical line shape is shown in Fig. 8. This trace was obtained while the laser cavity was arranged in the dual-frequency configuration. The laser was operating on both the $P(20)$ and $R(10)$ transitions in the 10.6-μm 961-cm^{-1} band. Measurements show that the $P(20)$ pulse contained about 40% more energy than the $R(10)$ pulse. It is easy to distinguish the allowed 4713-Å line, the satellite produced by the $P(20)$ line and the additional $R(10)$ satellite. The difference in satellite intensities is caused not only by the difference in energy in the two pulses, but also by the fact that the $R(10)$ transition is twice as far from resonance as the $P(20)$ transition [that is, $\Delta_{R(10)} = 2\Delta_{P(20)}$; see Eqs. (2.12) and (2.15b)]. The asymmetry of the allowed line and satellites is striking evidence of the Stark repulsion of levels diagrammed in Fig. 4. The instrument width for these traces was approximately 0.45 Å. The extreme broadening of these lines is primarily because of the spatial inhomogeneity of the laser pulses. Three-photon effects involving, for example, an optical photon, a $P(10)$ photon, and a $P(20)$ photon have been observed and will be discussed in a future publication. This phenomenon produces two spectral lines flanking the allowed line and separated from it by $\pm(\hbar\Omega_{P(10)} - \hbar\Omega_{P(20)})$.

IV. EXPERIMENTAL RESULTS AND COMPARISONS WITH THEORY

In order to compute the line shape of the atomic system discussed in the previous sections, we must first incorporate the level degeneracies into the theory. In the presence of the electric field the $|nlm_l\rangle$ representation is the most accurate.[22] The $4\,^3P$ level is found to be threefold degenerate ($m = 0, \pm 1$), while the lower level is nondegenerate ($m = 0$). We assume that the electric field is polarized in the Z direction and thus allow an interaction only between $m = 0$ states. This is equivalent to averaging over m states. We thus assume that only the $m = 0$ states show any Stark shift or two-photon effects. We also assume that the three levels of the $4\,^3P$ state are closely coupled collisionally. Since the various m levels are nearly degenerate, they must have equal populations at all times. In terms of the notation presented in Sec. II, $N_{4^3P} = K[3(\eta_a + \zeta_b)]$, where N_{4^3P} is the total population of the $4\,^3P$ level and K is a field-dependent normalization factor. We may then also write $N_{4^3S} = K(\eta_b + \zeta_a)$. We assume that major collisional processes are not grossly affected by the presence of the laser field so that the total population of the $4\,^3P$, ^3S manifolds remain constant. Clearly, the

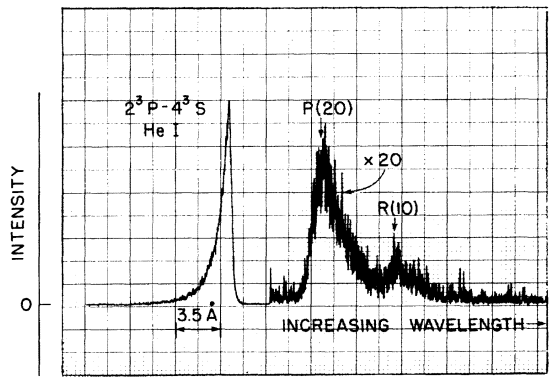

FIG. 8. Strip-chart recording of the 4713-Å He I line and two laser-produced satellites. The laser was operated in the dual frequency configuration on the $P(20)$ and $R(10)$ transitions of the 960.99-cm^{-1} band. The average electric field strengths were 120 and 100 kV/cm, respectively. The instrument width was 0.45 Å.

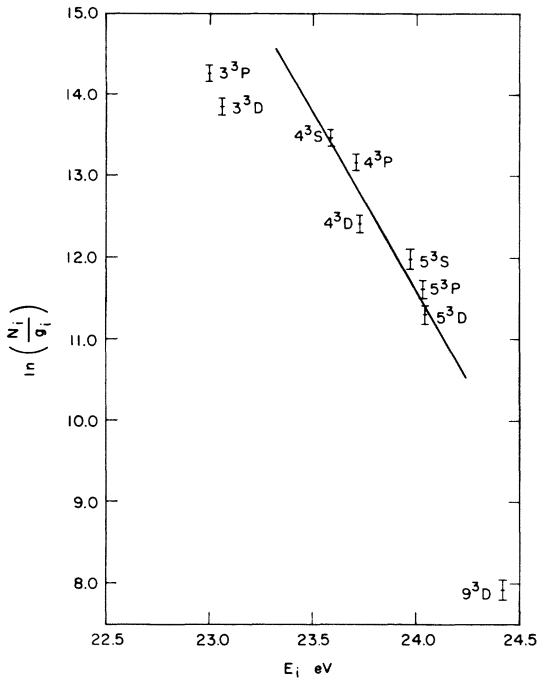

FIG. 9. Boltzmann plot of the triplet levels in helium. The straight line is characteristic of a Boltzmann distribution with a temperature of 0.2 eV.

total radiative rate out of these states is unperturbed by the laser field. This can be seen by using Eqs. (2.4) and (2.11).

We may now choose our normalization such that $K[3(\eta_a+\xi_b)+(\eta_b+\xi_a)]=1$, where $\eta_{a,b}$ and $\xi_{a,b}$ are functions of the electric field. Since this must be true for all field strengths, we have $K=[3(\eta_a+\xi_b)+(\eta_b+\xi_a)]^{-1}$. We thus include the degeneracies by premultiplying Eq. (2.17) by K, and adding an unshifted component $2(\eta_a+\xi_b)$ to the 3188-Å He I $4\,^3P$-$2\,^3S$ line to account for the $m=\pm 1$ upper states. The final states ($2\,^3P$, $2\,^3S$) are expanded into the $|nlm\rangle$ representation in order to compute the necessary matrix elements. We have used the energy levels and matrix elements given by Wiese *et al.*[23] in all of our calculations.

The degeneracies partially explain the large change in population of the $4\,^3S$ level illustrated in Fig. 7(b). The laser field tends to equalize the population of the $m=0$ states, but because of the degeneracies of the upper states, the $4\,^3S$ state must change three times as fast as the $4\,^3P$ state. In fact, when satellites are included, we find that although the 4713-Å line loses 35–40% of its intensity, the 3188-Å line shows almost no change, as expected.

We have measured the relative populations of some of the excited states of He I by comparing the intensities of various He emission lines and assuming that

$$I=(N_i A_\lambda/\lambda)\,K(\lambda). \tag{4.1}$$

I is the line intensity, N_i is the population of the upper state of the transition, A is the transition rate, λ is the transition wavelength, and the coefficient $K(\lambda)$ represents the sensitivity of the detection system and all relevant geometrical factors. In Fig. 9 we have plotted $\ln(N_i/g_i)$ vs E_i^0 for various helium states (g_i is the level degeneracy.) The result is a straight line characteristic of a Boltzmann distribution with a temperature of 0.2 eV. The electron temperature is about 3 eV. A non-Boltzmann distribution of excited states is not uncommon, since electron collisions are not the sole means of populating the states.[24]

We find from this plot that the ratio of a_0^2/b_0^2 is approximately 0.6. In Fig. 10 we have plotted the same excited-state densities as they appear with the laser radiation incident on the plasma. Although most of the levels change slightly, the major alteration is in the population of the $4\,^3P$ and $4\,^3S$ states. The circle (Fig. 10) indicates what the $4\,^3S$ density was without the laser. Note that the laser has equalized the populations of the $4\,^3S$ and $4\,^3P$ levels (within their degeneracies). As indicated by Eq. (2.15b), this population change is field-dependent, and will obviously have an effect on the

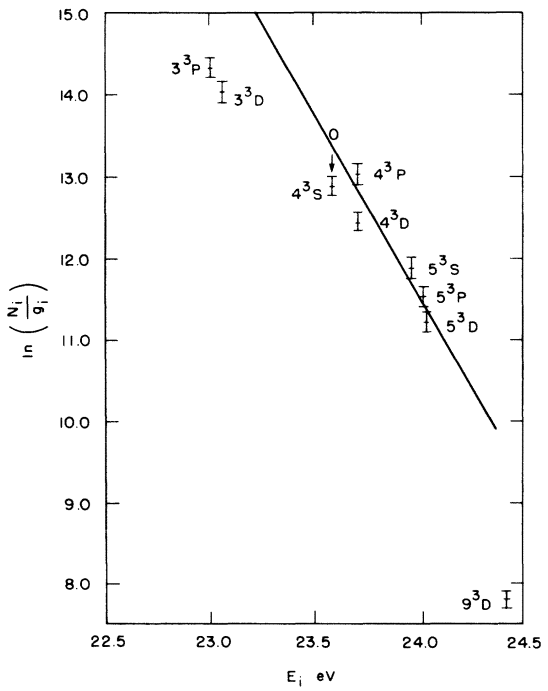

FIG. 10. Boltzmann plot of the triplet levels in helium as perturbed by the CO_2 laser field. Note the change in the $4\,^3S$ level, shown by the arrow, owing to the presence of the laser field.

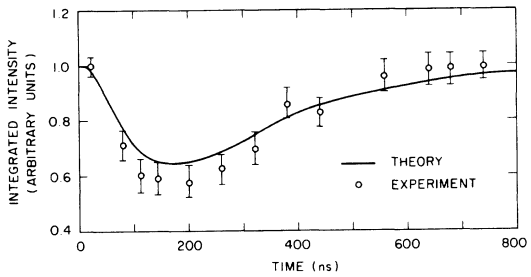

FIG. 11. Comparison of theory and experiment for the integrated intensity as a function of time of the 4713-Å line during the laser pulse.

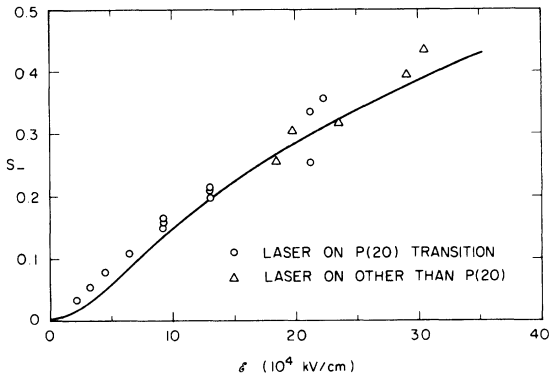

FIG. 12. Comparisons of the integrated intensity ratio of the near satellite to its accompanying allowed line S_-, as computed by using the rotating-wave approximation accounting for the electric field distribution $W(\epsilon)$ with the experimental results. The open triangles represent data taken on laser transitions other than $P(20)$.

line shape. The large change in population of the $4\,^3S$ level illustrated in Fig. 10 is the result of two processes. First, the intense laser field redistributes the population of the $4\,^3S$, ^3P states such that, at sufficiently high fields, the ratio of their populations would be given by the ratio of their degeneracies. Second, the satellite lines effectively reduce their allowed line intensities.

Figure 11 shows the measured integrated intensity of the He I 4713-Å allowed line for several different time intervals during the laser pulse and the calculated intensity given by integrating Eq. (2.17) over all values of ω. The data were obtained by adjusting the internal time delay of the boxcar integrator which was triggered at the beginning of the laser pulse. After the initial delay time, the photomultiplier output was sampled for 20 nsec while the monochromator was scanned through the 4713-Å allowed line. The total integrated intensity was then determined after a correction factor was taken into account for the instrument width (0.29 Å). The laser field strength as a function of time was determined from photographs of the laser pulse. The peak field was chosen to be 130 kV/cm. The method of choosing the peak field is explained below. The above results also depend on $W(\epsilon)$, which we calculated as described in Appendix A.

In Fig. 12 we have plotted the ratio of the integrated intensity of the satellite line to the integrated intensity of the associated allowed line at 4713 Å for several values of laser power. We have also included data resulting from tuning the laser to transitions other than $P(20)$ by scaling the laser power by $[(E_A - E_B - \hbar\Omega)/(E_A - E_B - \hbar\Omega_{P(20)})]^{-2}$. This accounts for the alteration in the resonant denominator of Eq. (2.12). We are able to measure the average energy in each pulse, but since not all of the energy is in the main peak, and since there are various unknown losses in the optical system, we do not have a precise measurement of the electric field in the capillary. In order to compensate for these unknown losses, ϵ_0, the average electric field (averaged over the discharge-tube cross section and the 200-nsec laser pulse width), was varied to fit the data for one value of measured average laser power. This relationship was then used to determine ϵ_0 for the remainder of the data from laser-power measurements. The data were taken

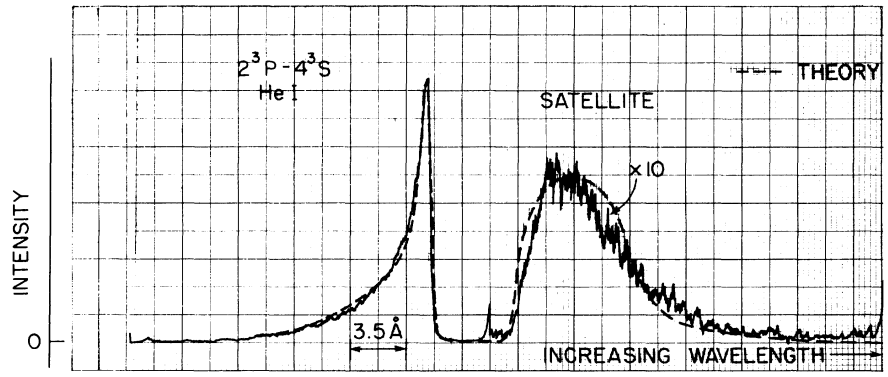

FIG. 13. Comparison of theory and experiment for the He I 4713-Å line and its associated satellite. The CO_2 laser was operated on the $P(20)$ transition with an average electric field of 130 kV/cm (Ref. 25).

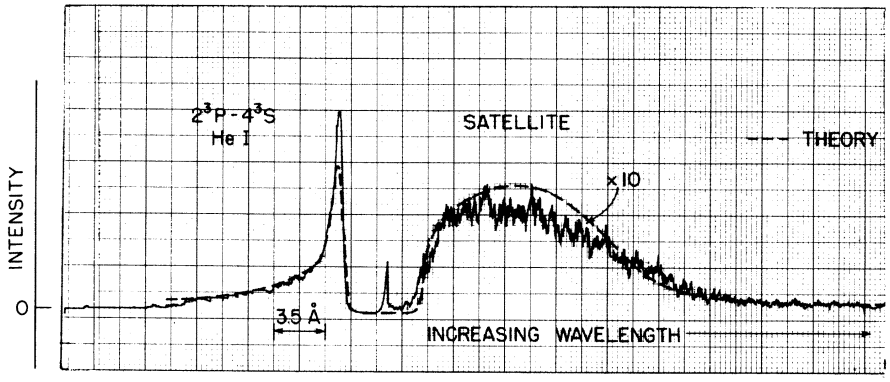

FIG. 14. Comparison of theory and experiment for the He I 4713-Å line and its associated satellite. The CO_2 laser was operated on the $P(20)$ transition with an average electric field of 221 kV/cm (Ref. 25).

on five different days over a period of two months. The field required to fit the data would require that approximately 30% of the power measured be in the main laser pulse 200 nsec wide. This is consistent with an examination of photographs of the laser pulse. Note that at higher field strengths the satellite intensity changes very slowly as saturation is reached.

Figures 13–16 demonstrate that the theory outlined in Sec. II is capable of describing satellite profiles over a wide range of parameters. Figure 13 and 14 are profiles of the $2\,^3P$-$4\,^3S$ allowed line and $2\,^3P$-$4\,^3P$ satellite line at two different field strengths. Figure 15 demonstrates the resulting line shape when the laser is tuned to the $P(34)$ transition (10.6-μm branch) instead of the $P(20)$ transition as in Figs. 13 and 14. This yielded an energy deficit of 12 cm^{-1} and was the closest we came to resonance. Figure 16 is an experimental trace of the $2\,^3S$-$4\,^3P$ (3188 Å) allowed line and $4\,^3S$-$2\,^3S$ satellite.

The theoretical curve drawn in Fig. 13 was computed for an average electric field strength ϵ_0 of 130 kV/cm. This value was chosen by using the power-to-field conversion ratio determined by Fig. 12, as explained above. We also used a value of 0.6 for a_0^2/b_0^2, as determined from Fig. 9. There were no additional parameters used to fit the line shape, although we did normalize the height of the theoretical curve to the height of the experimentally measured allowed line. No pressure broadening was included ($\gamma \to 0$) because both the $4\,^3S$ and $4\,^3P$ levels show very little broadening at the observed densities (7×10^{14} cm^{-3}). Spectral intensities were calculated every 0.18 Å and the result was convolved with the measured instrument function (including the averaging electronics and sine bar error). The final result is the curve shown in Fig. 13. As can be seen, a very good fit to the experimental data was then obtained. In the absence of the laser, the apparent width of the allowed line is that of the instrument function or approximately 0.45 Å.

In Fig. 14 we have presented a trace taken at a laser energy three times that of Fig. 13. Note that the allowed line has become broader and slightly less intense, while the satellite profile reveals a broad, flat top. This occurs because the field strength is large enough to cause the satellite in-

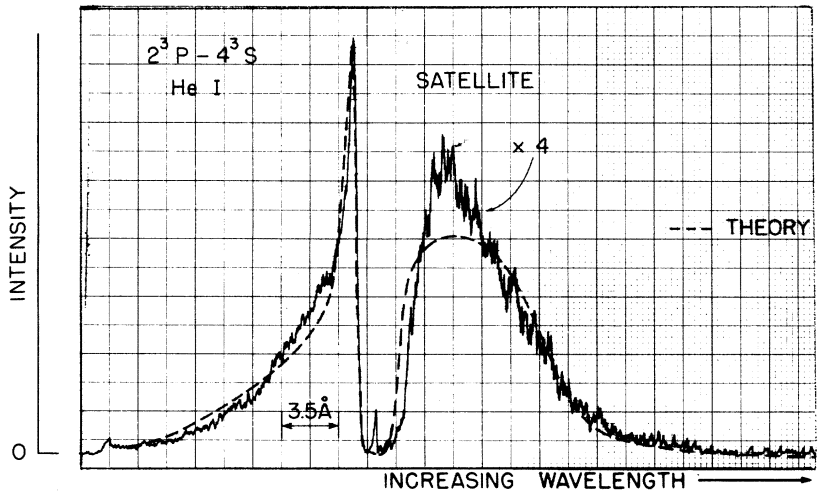

FIG. 15. Comparison of theory and experiment for the He I 4713-Å line and its associated satellite. The CO_2 laser was operated on the $P(34)$ transition with an average electric field of 145 kV/cm (Ref. 25).

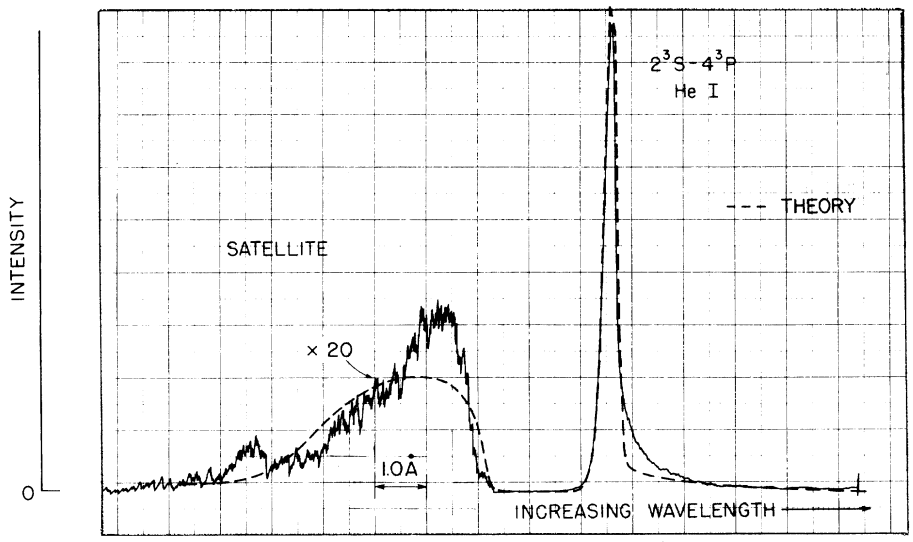

FIG. 16. Comparison of theory and experiment for the He I 3188-Å line and its associated satellite. The CO_2 laser was operated on the $P(20)$ transition with an average electric field of 130 kV/cm (Ref. 25).

tensity to saturate. Theoretical considerations would lead one to expect the satellite intensity to equal the allowed line intensity at saturation ($\tan^2\frac{1}{2}\chi \to 1$ as $\tan\chi \to \infty$). At first glance, Fig. 14 would not seem to represent this situation as the allowed line peak is almost twenty times greater than the satellite peak. However, it must be remembered that $W(\epsilon)$ weights various portions of the line shape differently. If we compare the portion of the allowed line that is shifted from its unperturbed position by 6 Å (for example) with the portion of the satellite profile which is also shifted by 6 Å, we are able to compare intensities which have been weighted equally by $W(\epsilon)$. This is because the equal Stark shifts insure that these portions of the respective profiles originate from regions of equal electric field and therefore equal $W(\epsilon)$. Allowing for the scale ratio of 10:1, it now becomes obvious that the satellite and allowed line are almost equal in intensity and that the satellite is, in fact, nearly saturated. Also note that the satellite is almost 15 Å wide (between half-power points) in spite of the fact that the $4\,^3P$ level has a pressure-broadened width of less than 0.1 Å at these densities. The width is the result of the laser-induced ac Stark shift.

The theoretical curve shown in Fig. 14 was obtained without the use of any free parameters. The intensity normalization was the same as that of Fig. 13, $a_0^2/b_0^2 = 0.6$, and the average field of 221 kV/cm (corresponding to a peak field of 800 kV/cm) was determined from the laser-power measurements. The satellite shape is well described, but the theoretical predictions for the allowed line are not as good. The theory predicts too large a Stark shift for the allowed line, although the integrated intensity is approximately correct. The reasons for this error are not clear, but two possibilities are most likely. First, there are probably slight inaccuracies in $W(\epsilon)$ which become apparent only at large field strengths. Second, the error could be the result of the interference of many other levels which are not included in the three-level theory of Sec. II. Individually, these levels might seem unimportant, but the total of all their contributions might account for the observed discrepancy.

The interaction may be made stronger by tuning the laser closer to resonance rather than increasing the field strength. Figure 15 demonstrates what happened when this was done. The field was approximately 145 kV/cm, but since the laser was operating on the $P(34)$ transition of the 10.6-μm branch, the value of $\tan\chi$ was actually 35% larger than that of Fig. 13. This is evident from the fact that the satellite in Fig. 15 is greater than that of Fig. 13. The line shape is also slightly altered. This is because at large field strengths the Stark shift becomes linear in ϵ and independent of the energy deficit.

The theoretical curve drawn in Fig. 15 was computed in the same manner as those shown in Figs. 13 and 14. The intensity normalization has remained the same, i.e., there has been no change in any parameters except the field strength (altered according to power measurements) and field frequency (measured by the CO_2 spectrum analyzer). It is interesting to note that the Baranger and Mozer perturbation result yields an $S_- \approx 19$ for the experimental parameters shown in Fig. 15. The perturbation theory would obviously be completely inadequate to predict the line shape. The reasons for the discrepancies between theory and experiment in Fig. 15 are almost certainly the same as

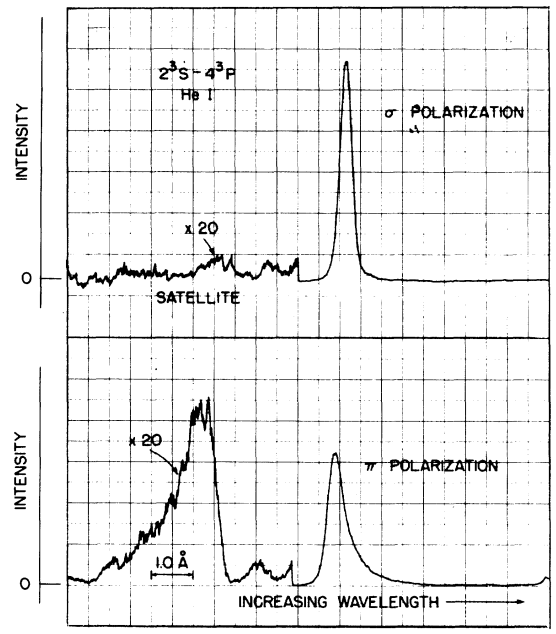

FIG. 17. Recorder traces of the He I 3188-Å allowed line and its associated satellite showing both the π and σ polarization components.

those mentioned in reference to Fig. 14, i.e., additional contributing levels and inaccuracies in the form of $W(\epsilon)$.

A trace of the $2\,^3S$-$4\,^3P$ (3188 Å) allowed line and $2\,^3S$-$4\,^3S$ satellite is shown in Fig. 16. The field strength is 135 kV/cm. The satellite is now observed on the low-wavelength side of the allowed line instead of on the high-wavelength side as expected. The slight irregularity on the tail of the satellite is caused by an impurity line. The resolution was better in this trace (instrument width $\approx$0.25 Å) because the monochromator was operated in second order.

The satellite is seen to be a mirror image of the satellite in Fig. 13, as we would predict. The 3188-Å allowed line, however, is not the mirror image of that of Fig. 13. This is a consequence of the different degeneracies of the $4\,^3S$ and $4\,^3P$ states. Only the $m=0$ level of the $4\,^3P$ state interacts with the $m=0$ $4\,^3S$ state, and therefore only $\frac{1}{3}$ of the $4\,^3P$ level shows any Stark shift. All of the $4\,^3S$ state is shifted by the laser field. This explains why the $2\,^3P$-$4\,^3S$ (4713 Å) line is broadened to a greater extent by the laser than the $2\,^3S$-$4\,^3P$ (3188 Å) line.

Once again the theoretical curve was obtained without any renormalization. Corrections were made for the difference in detector sensitivity [Eq. (4.1)] at the different wavelengths. The difference in transition rates between the $2\,^3P$-$4\,^3S$ and $2\,^3S$-$4\,^3P$ lines was also included in the normalization of Fig. 16. The agreement between theory and experiment is once again seen to be good, although it still appears that too large a Stark shift is predicted for the $m=0$ component of the allowed line. An additional source of error in computing this line shape comes from failing to account properly for the direction of photon emission (θ; see Appendix B). The nature of the discharge tube makes this factor difficult to compute.

The line shape discussed above (Fig. 16) demonstrates that only the $m=0$ states interact with the laser field. This can be demonstrated in another manner. Photons emitted when transitions between $\Delta m=0$ states take place, are polarized in the π direction (parallel to the z axis or, in this case, the laser electric field). The 3188-Å line and the $2\,^3S$-$4\,^3S$ satellite should therefore show strong polarization effects. The precise details of the calculations are contained in Appendix B. As can be seen from Eqs. (B9) and (B10), the $2\,^3S$-$4\,^3S$ satellite is 100% polarized. Experimentally, we find that the satellite is approximately 90% polarized. This measurement is consistent with estimates of the laser polarization.

Figure 17 illustrates the σ and π components of the 3188-Å allowed line and its associated satellite. Note that the π component of the allowed line is now a mirror image of the 4713-Å allowed line (Fig. 13). It was the $m\neq 0$ components that altered the line shape in Fig. 16. The trace of the σ component (Fig. 17) does not show any laser-induced perturbations; there is no satellite line, and the allowed line does not reveal laser broadening. In this experiment the particular choice of levels makes the effect larger than that predicted by Cooper and Ringler.[2]

Satellites of the $2\,^1P$-$4\,^1S$ (5048 Å) allowed line have also been detected, but since the energy deficit is much larger in this case, the satellites are much weaker. The behavior of these satellites is also in agreement with our theoretical description.

On the basis of the results presented in this section, we can state that the rotating-wave approximation not only is justified, but also enables us to describe satellite-line profiles accurately in a regime where a perturbation treatment would be totally inadequate and a complete Autler-Townes treatment very tedious. The integrated intensity ratios are also well predicted. It does appear, however, that at high field strengths the three-level theory used here predicts a Stark shift that is larger than the one actually observed.

ACKNOWLEDGMENTS

The authors are grateful to Professor H. Griem and Professor J. Cooper for their helpful com-

ments and criticisms on this paper. The authors also wish to thank William J. Mulligan for designing and constructing the CO_2 laser used in this experiment.

APPENDIX A

In this appendix we calculate the electric field distribution $W(\epsilon)$ of the laser as it propagates along the waveguide described in Sec. III. We assume that the incoming beam is a Gaussian characterized by a waist size of radius w_0. The time-averaged electric field of the laser in free space, ϵ_g, may be written in the following manner:

$$\epsilon_g = \left(\frac{2}{\pi}\right)^{1/2} \frac{1}{w_0} L_p\left(\frac{2r^2}{w_0^2}\right) \exp\left(\frac{-r^2}{w_0^2}\right), \tag{A1}$$

where both the radial coordinate r and the waist size w_0 have been normalized to the tube radius a, and L_p is the Laguerre polynomial of degree P. Our laser operates in the fundamental TEM_{00} mode so that $L_p(2r^2/w_0^2) = 1$. Equation (A1) is normalized such that $\int_0^\infty dr\, \epsilon_g \epsilon_g 2\pi r = 1$.

We compute $W(\epsilon)$ by allowing the linearly polarized Gaussian to excite the normal modes of the dielectric waveguide, and then allow these modes to propagate coherently along the capillary guide. The normal modes of the cylindrical tube (r, θ, x coordinates) with differing internal and external dielectric constants are well known. We assume that the presence of the plasma causes no change in the index of refraction since the laser frequency is much greater than the plasma frequency. Stratton,[26] and later Marcatili and Schmeltzer,[27] have shown that there are three different types of modes, each characterized by its nonzero field components. These are the transverse circular electric modes (TE_{0m}, E_θ, H_R, $H_z, \neq 0$), transverse circular magnetic (TM_{0m}, H_θ, E_R, $E_z, \neq 0$), and finally the hybrid EH_{nm} modes (Marcatili and Schmeltzer notation) which have all six components present. None of the fields are zero at the tube walls ($r = 1$) since the capillary is actually a leaky waveguide which allows some of the power to escape through the walls. This loss is extremely small for our geometry, since if $\lambda/a << 1$ (where λ is the free-space wavelength), the terms which are nonzero at the walls may be ignored. This condition is well satisfied. When one ignores terms of order λ/a, it becomes apparent that the EH_{1m} modes are linearly polarized. As the laser is also linearly polarized, it is reasonable to assume that the EH_{1m} modes (Degnan and Hall[28] notation—LP_{0m}) are preferentially excited by the laser. (Other combinations of modes are also linearly polarized, but these have an azimuthal variation and thus would not be excited by the fundamental Gaussian mode.) Because of this we will ignore all of the other capillary modes and write

$$\epsilon_m = J_0(u_{0m} r) \exp i(k_m x - \omega t), \tag{A2}$$

where J_0 is the zeroth-order Bessel function $J_0(u_{0m}) = 0$,

$$k_m = \frac{2\pi}{\lambda}\left[1 - \tfrac{1}{2}\left(\frac{u_{0m}\lambda}{2\pi a}\right)^2\right] \tag{A3}$$

and terms of order λ/a have been ignored (except in the exponential phase factor where they are much more important).

We now follow a standard technique[29] and compute the field in the waveguide as a linear combination of the normal modes of the dielectric cylinder,

$$\epsilon = \sum_m G_m \epsilon_m. \tag{A4}$$

We impose the boundary conditions that at $x = 0$ the field must be a Gaussian [Eq. (A1)]. Solving for G_m, we find that

$$G_m = \frac{2}{[J_0'(u_m)]^2} \int_0^1 r J_0(u_m r) \exp\left(\frac{-r^2}{w_0^2}\right) \frac{\sqrt{2}}{\pi} \frac{1}{w_0}\, dr. \tag{A5}$$

We use a 16-point numerical Gaussian quadrature integration routine to calculate G_m for various values of w_0. The fundamental capillary mode is largest for $w_0 = 0.625$. This compares to 0.6435 as calculated by Abrams[29] for maximum coupling from the EH_{11} mode to the fundamental Gaussian. The energy coupled into mode m is found to be

$$U_m = G_m^2 \pi J_m'(u_{0m})/w_0^2. \tag{A6}$$

If w_0 is small, the energy is well distributed among many high-order modes so that only a small portion of the total is contained in the first four normal modes. If w_0 is large, the beam is truncated so that only a small portion of the energy is effectively coupled into the guide. If, however, w_0 is between 0.2 and 0.7, over 92% of the energy is found in the first four modes with the remainder distributed over many higher-order modes. As w_0 for the experiment discussed does indeed fall in this range, we feel justified in including only the four lowest-order modes.

Once the G_m are known, we may calculate the electric field for all points (r, x) in the capillary using Eq. (A2). After performing a time average, $W(\epsilon)$ can be easily expressed as a geometric weighting factor. It is the volume in which the electric field of strength ϵ is found. Figure 18 presents the results of this calculation when $w_0 = 0.4$. The distribution is normalized so that $\int W(\epsilon)\, d\epsilon = \pi$.

Several factors contribute to smooth out the dis-

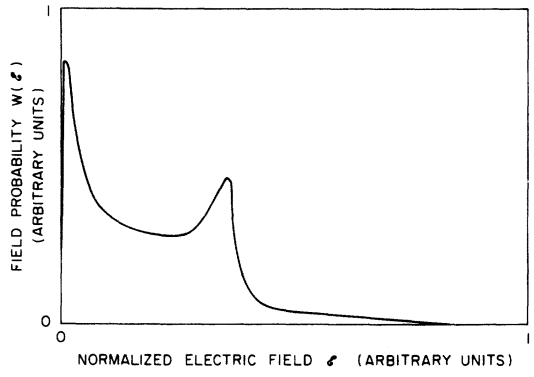

FIG. 18. Field probability $W(\epsilon)$ for $w_0 = 0.4$ as a function of the normalized electric field.

tribution shown in Fig. 18. First, the laser power fluctuates by approximately 10% from pulse to pulse. Second, the boxcar integrator samples the time variant laser pulse for 200 nsec during which the electric field changes by 50%. Both of these factors were incorporated before the line shape was calculated. Finally, the excited-state density profile $N(r)$ must be considered. We take this to be uniform except near the walls, where we let $N(r)$ go very rapidly to zero. Webb[30] has shown this to be a very good approximation. We have found, as expected, that the line shape does not depend critically on the form of $N(r)$ near the wall. This is a result of the small electric field near the walls.

We should point out that the calculations described above give only an approximate form for $W(\epsilon)$. We wish to see if we can predict the major features of the line shape with the field distribution described, but the many simplifications should be borne in mind. For example, we ignored the possible effects of the taper at the imput of the waveguide. We have ignored any possibility of irregularities in the capillary discharge tube that might effect the mode structure. All of these factors might explain why we measured 80–85% transmission through the tube when our calculations indicate that it should be 95%. The major features of the distribution are correct, and the line shape is not critically dependent on the other factors. We feel therefore that we are justified in using the distribution function as calculated above.

APPENDIX B

The polarizations of the $2\,^3P$-$4\,^3P$ and $2\,^3S$-$4\,^3S$ satellite transitions are calculated in this appendix. Following Cooper and Ringler,[2] the two-photon transition rate (A) from level A to level C may be written

$$dA_{AC} = \sum_{m_C} \frac{e^2}{8\pi\hbar^3 c^3}(\omega_{AC} \pm \Omega)\left(\frac{\omega_{BC}}{\omega_{BC} \pm \Omega}\right)^2 \times \sum_{m_B} 2\epsilon^2 |d_{AB}|^2 |d_{BC}|^2 d\phi, \tag{B1}$$

where $d\phi$ is the differential solid angle into which the photon is emitted, the summation over m_C is a sum over the m levels of the final state, and the summation over m_B is a sum over the m levels of the intermediate state. If we now define the Z axis to be parallel to the laser field we may write

$$|d_{AB}|^2 = e|Z_{AB}|^2, \tag{B2}$$

$$|d^{\pi}_{BC}|^2 = \tfrac{1}{2}(|X_{BC}|^2 + |Y_{BC}|^2)\cos^2\theta + |Z_{BC}|^2 \sin^2\theta, \tag{B3}$$

$$|d^{\sigma}_{BC}|^2 = \tfrac{1}{2}(|X_{BC}|^2 + |Y_{BC}|^2). \tag{B4}$$

In these equations, θ is the angle (relative to the Z axis) at which the photon is emitted. Equation (B3) is to be used when the photon is polarized parallel to the Z axis (electric field axis). Equation (B4) is to be used when the emitted photon is polarized perpendicular to the electric field axis.

If we now consider transitions of the form $l+1 \rightarrow l \rightarrow l+1$ (e.g., $4\,^3P$-$4\,^3S$-$2\,^3P$) and use the expressions for the X, Y, and Z matrix elements given by Bethe and Salpeter[22] the summations may be evaluated. The result is

$$\sum_{m_C m_B} |Z^{nl\,m_B}_{nl+1\,m_B}|^2 \frac{(|X|^2 + |Y|^2)^{n'l+1\,m_C}_{nl\,m_B}}{2} = \frac{1}{2}\left(\frac{(l+1)(12l^3+57l^2+71l+30)}{15(2l+1)(2l+3)^2}\right)(R^{nl}_{nl+1}R^{n'l+1)^2}_{nl}, \tag{B5}$$

$$\sum_{m_C m_B} |Z^{nl\,m_B}_{nl+1\,m_B}|^2 |Z^{n'l+1\,m_C}_{nl\,m_B}|^2 = \frac{l+1}{15}\left(\frac{4l^2+8l+5}{(2l+3)(2l+1)}\right)(R^{nl}_{nl+1}R^{n'l+1)^2}_{nl}, \tag{B6}$$

The $R^{nl}_{n'l'}$ are the radial integrals used by Bethe and Salpeter.[22] Now to study the $4\,^3P$-$2\,^3P$ satellite polarization, let $l = 0$. Then

$$dA^{\pi}_{2^3P-4^3P} = dA^{\sigma}_{2^3P-4^3P} = \frac{e^4}{9}\frac{\omega^3_{AC}}{\hbar^3 c^3}\frac{(R^{nl}_{nl+1}R^{n'l+1)^2}_{nl}}{(\omega \pm \Omega)^2}d\phi. \tag{B7}$$

There is no angular dependence and the satellite is unpolarized. [In Eq. (B7) the assumption that $\omega_{AC} \pm \Omega \approx \omega_{BC}$ was made to clarify the results]. If one now integrates Eq. (B7) over all solid angles, sums over both polarizations, and divides by

$$A_{BC} = \tfrac{4}{3}\omega^3_{BC}e^2|R^{2^3P}_{4^3S}|^2, \tag{B8}$$

the Baranger and Mozer result is recovered.

In a similar manner we may show that

$$dA^{\pi}_{2^3S-4^3S} = \frac{1}{9}\frac{e^4\omega_{AC}^3}{\hbar^3 c^3}\frac{1}{(\omega \pm \Omega)^2} \times |R^{4^3P}_{4^3S}|^2 |R^{2^3S}_{4^3P}|^2 \sin^2\theta \, d\phi, \quad \text{(B9)}$$

$$dA^{\sigma}_{2^3S-4^3S} = 0. \quad \text{(B10)}$$

These equations demonstrate that the $2\,^3S$-$4\,^3S$ satellite is 100% polarized and exhibits a strong angular dependence. If we integrate (B9) over all solid angles we find $A_{2^3P-4^3P} = 3A_{2^3S-4^3S}$, as expected. As indicated in Sec. IV, the polarization of the $2\,^3S - 4\,^3S$ satellite has been found to be greater than 90%. Note also that the shape of the $2\,^3S - 4\,^3P$ allowed line depends on polarization. The shifted component is polarized in the π direction.

---

*Work performed under National Science Foundation Grant No. ENG75-06242 and Joint Services Electronics Program Contract DAAB07-75-C-1346.

†Present address: Mason Laboratory, Yale University, New Haven, Conn. 06520.

‡Present address: Lawrence Livermore Laboratory, Livermore, Calif. 94550.

[1]M. Baranger and B. Mozer, Phys. Rev. 123, 25 (1961).

[2]W. S. Cooper, III, and H. Ringler, Phys. Rev. 179, 226 (1969).

[3]W. W. Hicks, R. A. Hess, and W. S. Cooper, Phys. Rev. A 5, 490 (1972).

[4]For a compendium of references on this subject, see H. R. Griem, *Spectral Line Broadening by Plasmas* (Academic, New York, 1974).

[5]D. Prosnitz and E. V. George, Phys. Rev. Lett. 32, 1282 (1974).

[6]Y. Hamada, J. Phys. Soc. Jpn. 29, 463 (1970).

[7]I. I. Rabi, Phys. Rev. 51, 652 (1937).

[8]S. H. Autler and C. H. Townes, Phys. Rev. 100, 703 (1955).

[9]M. Baranger, Phys. Rev. 111, 481 (1958).

[10]D. Prosnitz, Ph.D. thesis (MIT, 1975) (unpublished).

[11]J. H. Shirley, Phys. Rev. 138, B979 (1965).

[12]A. Javan, Phys. Rev. 107, 1579 (1957).

[13]F. Bloch and A. Siegert, Phys. Rev. 57, 522 (1940).

[14]A. S. Davydov, *Quantum Mechanics*, translated by I. V. Schensted (Neo Press, Ann Arbor, Mich., 1966).

[15]A. M. Bonch-Bruevich and V. A. Khodovoi, Usp. Fiz. Nauk. 93, 71 (1967) [Sov. Phys.-Usp. 10, 637 (1968)].

[16]H. R. Griem, Ref. 4, p. 157.

[17]R. Mewe, Brit. J. Appl. Phys. 18, 107 (1967).

[18]A. J. Bernard, J. Cooper, and L. J. Shamey, Astron. Astrophys. 1, 28 (1969).

[19]P. Platz, Appl. Phys. Lett. 16, 70 (1970); 17, 537 (1970).

[20]J. P. Kaplafka, M. Merkelo, and L. Goldstein, Appl. Phys. Lett. 19, 197 (1971).

[21]J. Chapelle, B. Dubreuil, H. W. Drawin, and F. Emard, Phys. Lett. 44A, 201 (1973); H. W. Drawin, F. Emard, B. Dubreuil, and J. Chapelle, Report EUR-CEA-FC-729 (Euratom-CEA, Fontenay-Aux Rose, 1974).

[22]H. A. Bethe and E. E. Salpeter, *Quantum Mechanics of One and Two Electron Atoms* (Academic, New York, 1957).

[23]W. L. Wiese, M. W. Smith, and B. M. Glennon, *Atomic Transition Probabilities*, NSRDS-NBS 4 (U.S. GPO, Washington, D.C., 1966).

[24]H. W. Drawin, High Temp.-High Pressures 2, 359 (1970).

[25]The electrical noise generated by the CO_2 laser causes a spurious signal when the screened room is opened to change the amplifier gain.

[26]J. A. Stratton, *Electromagnetic Theory* (McGraw-Hill, New York, 1941), p. 524.

[27]E. A. J. Marcatili and R. A. Schmeltzer, Bell. Syst. Tech. J. 43, 1783 (1964).

[28]J. J. Degnan and D. R. Hall, IEEE J. Quantum Electron. QE-9, 901 (1973).

[29]R. L. Abrams, IEEE J. Quantum Electron. QE-8, 838 (1972); A. N. Chester and R. L. Abrams; Appl. Phys. Lett. 21, 576 (1972).

[30]C. E. Webb, J. Appl. Phys. 39, 5441 (1968).

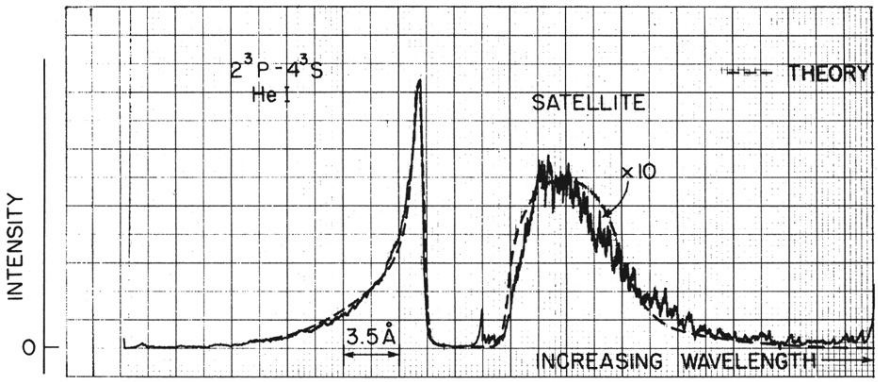

FIG. 13. Comparison of theory and experiment for the He I 4713-Å line and its associated satellite. The CO_2 laser was operated on the $P(20)$ transition with an average electric field of 130 kV/cm (Ref. 25).

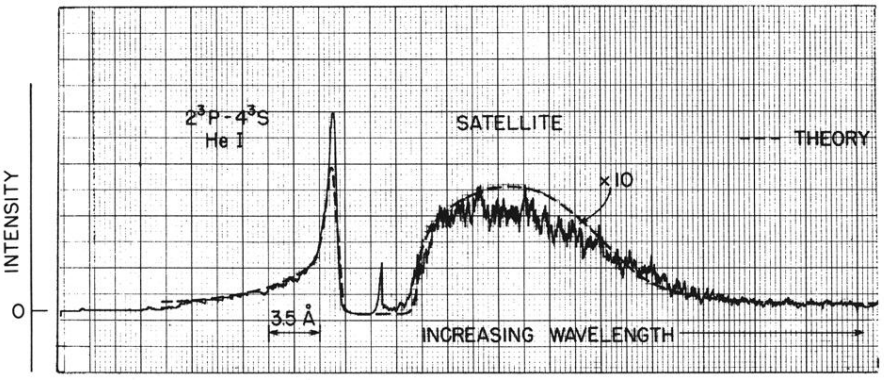

FIG. 14. Comparison of theory and experiment for the He I 4713-Å line and its associated satellite. The CO_2 laser was operated on the $P(20)$ transition with an average electric field of 221 kV/cm (Ref. 25).

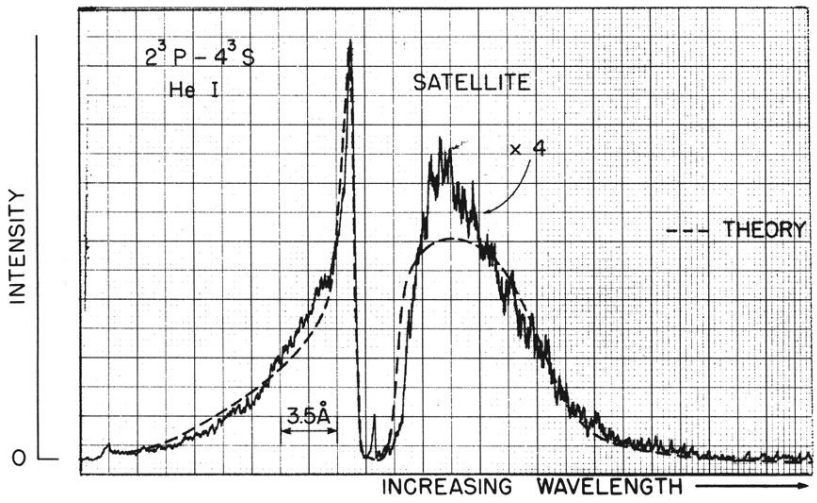

FIG. 15. Comparison of theory and experiment for the He I 4713-Å line and its associated satellite. The CO_2 laser was operated on the $P(34)$ transition with an average electric field of 145 kV/cm (Ref. 25).

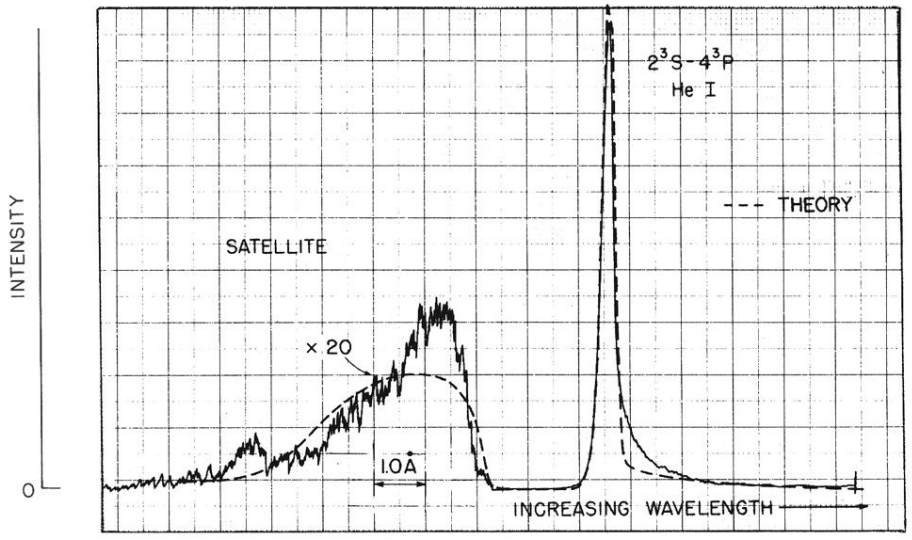

FIG. 16. Comparison of theory and experiment for the He I 3188-Å line and its associated satellite. The CO_2 laser was operated on the $P(20)$ transition with an average electric field of 130 kV/cm (Ref. 25).

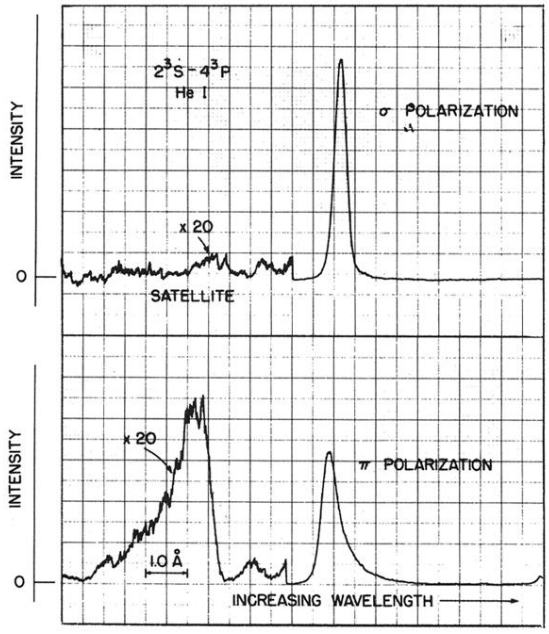

FIG. 17. Recorder traces of the He I 3188-Å allowed line and its associated satellite showing both the π and σ polarization components.

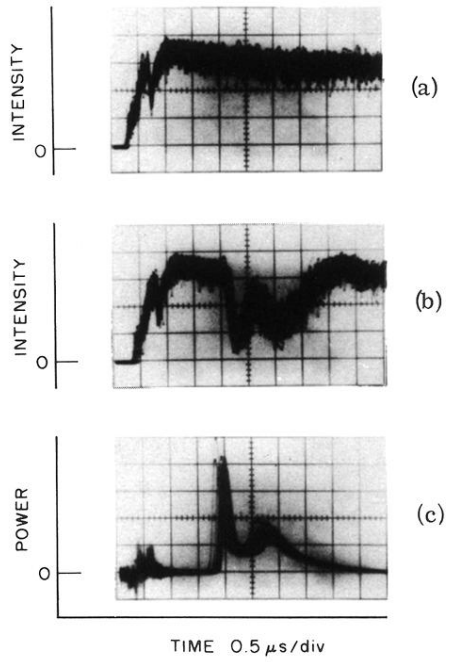

FIG. 7. Oscilloscope traces of (a) 4713-Å light pulse unperturbed by the laser (top trace), (b) 4713-Å light pulse perturbed by the laser (middle trace), and (c) laser pulse shape (bottom trace).

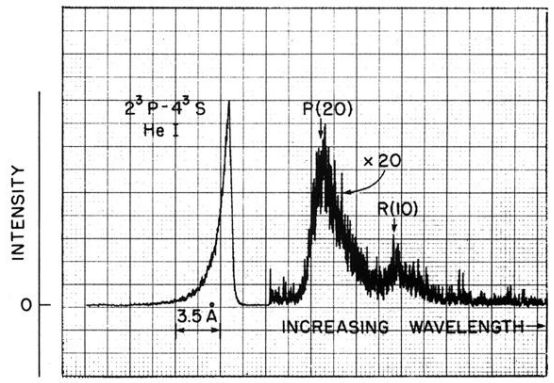

FIG. 8. Strip-chart recording of the 4713-Å He I line and two laser-produced satellites. The laser was operated in the dual frequency configuration on the $P(20)$ and $R(10)$ transitions of the 960.99-cm^{-1} band. The average electric field strengths were 120 and 100 kV/cm, respectively. The instrument width was 0.45 Å.